RSC Advances

PAPER

View Article Online
View Journal | View Issue

Cite this: *RSC Adv.*, 2023, **13**, 21781

Controlled synthesis and computational analysis of gold nanostars for the treatment of *Fusarium oxysporum*†

Gaddi B. Eshun,[a] Francis J. Osonga,[a] Taner Erdogan,[b] Ayşegül Gölcü[c] and Omowunmi A. Sadik *[a]

Fusarium oxysporum (*F. oxysporum*) is linked to the widespread fusarium wilt in plants affecting the quality and yield of food crops. Management of fusarium wilt by synthetic fertilizers poses safety concerns. Safer-by-design nanomaterials synthesized with a greener approach can meet the needs of commercial antifungal drug resistance. Herein, a simple aqueous reduction method has been adopted for the synthesis of anisotropic gold nanostars (AuNSs) using quercetin-*para* aminobenzoic acid (QPABA) as both a reducing and stabilizing agent at room temperature for the treatment of *F. oxysporum*. QPABA was used to control the growth of Au^{3+} star-shaped nanoparticles at increasing concentrations in the ratio of 2 : 1 (QPABA : Au^{3+} ions) respectively. Transmission electron microscopy (TEM) analysis of the as-prepared gold nanoparticles confirmed the formation of nanostars with sizes of 40 ± 2 nm. The formation of anisotropic gold nanoparticles was evaluated by UV-vis characterizations which showed longitudinal surface plasmon modes at 540 and 800 nm. The gold nanoparticles exhibit excellent antifungal activity against *F. oxysporum* with the minimum inhibitory concentration (MIC) of 100 μg mL^{-1} using an agar well-diffusion assay. AuNSs proved to be efficacious in controlling *F. oxysporum*, as shown in the SEM analysis with a disintegrated cell membrane upon treatment. Computational analysis was performed to determine the specific binding sites on the QPABA ligand for gold ion interactions using the DFT B3LYP method, with a 6-31+G(d) basis set. Results showed that the interaction between Au^{3+} and QPABA at the 4 and 3 positions yielded the highest stability and formation of gold nanostars. The results suggest that the synthesized AuNSs act as a promising antifungal agent with great potential in treating frequent fungal infections that affect agricultural production.

Received 17th June 2023
Accepted 6th July 2023

DOI: 10.1039/d3ra04088g

rsc.li/rsc-advances

1 Introduction

Fusarium oxysporum is responsible for the infectious wilt diseases that affect plants. Fusarium wilt is a soil-borne pathogen that produces mycotoxins that attack sweet potato, tomato, and eggplant products.[1,2] The impact of wilt diseases on food crops introduces economic burdens and devastating crop losses to agricultural production. Some chemical pesticides[3] are commonly applied to manage wilt diseases.[2,4,5] However, the excessive use of chemical pesticides against wilt diseases possibly gives rise to residual toxicity, fungal resistance, environmental pollution, and health hazards. To avoid this predicament, the application of safe biocontrol agents holds promise for treating wilt diseases as compared to toxic pesticides.[4,6] Nanomaterials such as silver, gold, and copper nanoparticles (NPs) offer an ideal treatment against *F. oxysporum*. Nevertheless, the toxicity of the nanomaterials has been a concern in designing antifungal nano agents.[7] In this study, gold nanostar synthesized from greener quercetin derivative (QPABA – (4,4′,4″-((2-(3,4-bis((4-carboxyphenyl)amino)phenyl)-4-oxo-4*H*-chromene-3,5,7-triyl)tris(azanediyl))tribenzoic acid)) is applied as an antifungal owing to its morphology, small surface-to-volume ratio, and biocompatibility with low toxicity.

Nanomaterials are attractive materials due to their promising application in various fields, such as optics, electronics, catalysis, and biomedicine.[7–9] Physical and chemical methods are widely used in the production of nanomaterials.[10–12] The development of greener reducing and capping agents for synthesizing gold NPs is the focus of modern nano synthesis.[13,14] Gold nanoparticles' unique and tunable properties are promising tools for diverse biomedical applications such as drug treatment, gene therapy, and diagnostic methods.[15] To date, enormous efforts have been dedicated to

[a]*Department of Chemistry and Environmental Science, New Jersey Institute of Technology, University Heights, 151 Warren Street, Newark, NJ, 07102, USA. E-mail: omowunmi.sadik@njit.edu*

[b]*Kocaeli Vocat Sch, Department of Chemistry and Chemical Processing Technologies, Kocaeli University, Kocaeli 41380, Turkey*

[c]*Department of Chemistry, Faculty of Science and Letter, Istanbul Technical University, Istanbul 34469, Turkey*

† Electronic supplementary information (ESI) available. See DOI: https://doi.org/10.1039/d3ra04088g

controlling the size and shape of gold nanomaterials using the greener methodology. In this study, *para*-aminobenzoic acid was applied as a bioactive molecule to tune the shape-directing properties of gold nanoparticles[10,13,15]

The focus on gold nanostructures is attributed to their unique features such as biocompatibility, inertness, and low toxicity as compared to zinc oxide nanoparticles with high toxicity.[16] In general, nanoparticles possess a high surface area-to-volume ratio.[17] It is worth stating that the branching/spike morphology of the gold nanostar contributes to the high surface area-to-volume ratio[17] necessary for synthesizing an effective nano-fungicide. Furthermore, the branching/spike in gold nanostar possesses high-index facets that exhibit superior catalytic activity and can enhance the signals associated with surface-enhanced Raman spectroscopy (SERS).[18]

Natural amino acids such as *para*-aminobenzoic acid play a role as reducing and capping agents for the synthesis of anisotropic gold nanoparticles with biological applications.[19,20] However, the biosynthesis of nanomaterials is highly favorable due to the use of phytochemicals such as flavonoids.[21] Flavonoids are polyphenols with rich antioxidant properties. The antioxidant property of flavonoids is responsible for reducing metal ions during the synthesis of nanoparticles. Notably, Quercetin (Flavonoid) is partially insoluble in polar solvents with limited aqueous applications.[22] Quercetin is functionalized with *para*-aminobenzoic acid to improve its polar solubility. The resultant product, QPABA, is utilized as a capping and reducing agent for synthesizing gold nanostars.

Herein, we demonstrate the aqueous synthesis of gold nanostars using QPABA at room temperature without additional surfactants. The influence of QPABA on the size, morphology, and monodispersed gold nanostars was initiated by the 2 : 1 ratio of QPABA and gold metal precursor, respectively. Furthermore, spherical nanoparticles were obtained by the 1 : 1 ratio of QPABA and Au^{3+} ions. The growth process of gold nanostars was monitored using UV-vis spectroscopy and characterized with TEM, XRD, and EDX. The AuNSs showed excellent antifungal activity against *F. oxysporum* using the agar well-diffusion assay. The stability of the QPABA-Au^{3+} complex is proposed *via* DFT calculations for the interactions between Au^{3+} ions and possible binding sites within the QPABA ligand. The stability of the gold nanostars and their antifungal potency against *F. oxysporum* shows that the synthesized AuNSs could be adapted as a greener regimen for the treatment of agricultural fungal infections. The cost-effective synthesis and use of QPABA derived from the facile functionalization of quercetin promotes the sustainability of nanomaterial production.

2 Experimental section

2.1 Reagents

Anhydrous quercetin, hydrogen tetrachloroaurate salt ($HAuCl_4 \cdot 3H_2O$), and *para*-aminobenzoic acid were purchased from Sigma-Aldrich, Milwaukee, WI. Methanol, sodium hydroxide pellets, and hydrochloric acid were purchased from Fisher Scientific, Pittsburg, PA. Ultrapure water with a resistance of >18.2 MΩ cm was utilized for all the synthesis. *Fusarium oxysporum* was purchased from the American Type Culture Collection (ATCC 48112) (Manassas, VA). 100 mm Corning agar plates were purchased from Fisher Scientific, Pittsburg, PA. Potato dextrose broth was purchased from Oxoid Microbiology Products (Hampshire, UK).

2.2 Experimental characterizations performed on gold nanostars

The synthesized gold nanoparticles were characterized using an Agilent Cary 3500 Multicell UV-vis spectrophotometer. Transmission electron microscopy (TEM), and Selected Area Electron Diffraction (SAED) (JOEL 7100F) were applied for the analysis of the size, shape, and crystallinity of the anisotropic gold nanostars respectively. The TEM samples were prepared by drop-casting the gold nanoparticles on a carbon-coated copper grid and dried overnight. The XRD characterization was performed using Bruker D8 Advance 800234-X-ray operating at 40 kV within the scan range of 20–80°. The effects of anisotropic gold nanoparticles against *Fusarium oxysporum* were visualized using a Field Emission-Scanning Electron Microscope (FE-SEM) at an accelerating voltage of 10 kV. The EDX equipped with the TEM instrument was utilized for the determination of the atomic compositions of the anisotropic gold nanoparticles.

2.3 Synthesis of quercetin *para*-aminobenzoic acid (QPABA)

To enhance the polar solubility of quercetin, *para*-aminobenzoic acid (PABA) was used to functionalize quercetin *via* a two-step reductive amination. Briefly, 1 mmol of quercetin (QCR) (300.23 mg) was dissolved in 200 mL of methanol in a 500 mL reaction flask. A separate solution of 5 mmol (137.14 mg) *para*-aminobenzoic acid was made using a 70% acetic acid and 30% water mixture.[19] The resultant PABA mixture was added to the QCR mixture. 2 mL of HCl was added to facilitate the reaction and the excess acid was further neutralized using NaOH pellets. After 2 hours, 300 mg of dimethylamine borane was added, and the reaction then proceeded for 24 hours. The resultant QPABA product in solution was purified and thoroughly characterized using analytical techniques. Detailed characterization results have been reported in our previous work.[19]

2.4 Synthesis of AuNSs using QPABA at room temperature

To achieve the aqueous reduction of Au^{3+} to Au^0, QPABA was utilized as a bifunctional reducing and stabilizing agent. A standard 1 mM aureate solution ($HauCl_4 \cdot 3H_2O$) was prepared in a cleaned 50 mL vial. 5 mM of QPABA was also prepared in another 50 mL vial. In a one-pot chamber, 200 μl aliquots of gold and 200 μl of QPABA solution were reacted with the

Table 1 Concentration-dependent synthesis of AuNS at 25 °C

Vials	QPABA	Au^{3+} ions	Distilled water
A	200	200	1000
B	400	200	1000

addition of 1000 μl of distilled water at room temperature (25 °C). Table 1 shows the series of reaction setups for the synthesis of AuNSs. The spectrophotometric measurements of the samples were performed using Agilent Cary 3500 Multicell UV-Vis Spectrophotometer. AuNS were purified *via* centrifugation at 3500 rpm for 10 minutes and dried for further characterization.[19] Scheme 2 demonstrates the synthesis of anisotropic gold nanoparticles.

2.5 Computational analysis of AuNSs-derived QPABA

Computational studies were performed to determine the optimized geometry for QPABA. Before geometry optimization, a conformational analysis was performed on QPABA using VConf[23] and Gaussian 09 (ref. 24) software packages to obtain the most stable conformer. Furthermore, geometry optimization was performed using the DFT B3LYP method, 6-31+G(d) basis set, PCM solvation model, and water was selected as solvent. In this calculation, the GAMESS[25] software package was used. QPABA has five hydroxyls (–OH) groups that are binding sites in the structure. Since nanoparticles contain many metal atoms and are impossible to mimic *in silico*, only one Au atom was selected to determine its interaction with QPABA. Five nanocomposite structures were constructed by replacing the hydrogen atom of each hydroxyl group in QPABA at a time. After obtaining the structures, energy minimizations were performed on the structures with the use of the DFT B3LYP method, LANL2DZ basis set for Au, 6-31G(d,p) basis set for elements other than gold, IEFPCM solvation model was used. In these calculations, the Gaussian 09 (ref. 24) software package was used. GaussView20 and Discovery Studio Visualizer21 software packages were used to visualize the results. Furthermore, the angles around the Au^{3+} subsequently were preserved, and the interaction energy (stability) between Au^{3+} and QPABA was determined.

2.6 Preparation of cells

F. oxysporum spores (ATCC 48112) were cultured in the Peptone Dextrose Broth (PDB), and incubated at 28 °C overnight for 48 h. The cells were harvested by centrifugation and adjusted to 10^5 cells per mL. The antifungal activity of AuNSs was investigated in a dose-dependent manner. The concentration gradients of AuNSs (75, 100, 125 μg mL^{-1}) were transferred to the agar plates seeded with 10^5 cells per mL fusarium conidia. The plates treated with the AuNSs were then incubated at 28 °C overnight.

2.7 Agar well diffusion assay

To determine the antifungal potency of AuNSs against *F. oxysporum*, the agar well-diffusion method was adapted for this study.[26] Briefly, Molten PDA was obtained by dissolving 3.9 g of the PDA into 100 mL of ultrapure water in a 200 mL beaker. The PDA agar solution was autoclaved at 121 °C for 30 min. The PDA molten agar was then poured into a 100 mm Petri dish plates (Fisher Scientific), and the agar plates solidified in a biosafety hood. The yeast cells (100 μl mL^{-1}) were seeded onto the agar plates, followed by creating three equidistant 5 mm wells on each agar plate using a Cork borer.[26,27] Each agar plate was loaded with AuNSs (75 μg mL^{-1}, 100 μg mL^{-1}, and 125 μg mL^{-1}) in one experimental setup. QPABA in solution was used as the control. The antifungal potency of AuNS nanoparticles against *F. oxysporum* was determined from the zone of inhibition using the control as a reference. The plates were incubated at 28 ± 2 °C for 7 days. The zone of inhibition was calculated as a percentage[28] using the equation below:

$$\text{Antifungal inhibition (\%)} = (M_b - M_a)/M_b$$

where M_a is the diameter of the inhibition zone around the wells (mm) and M_b is the diameter of the inhibition zone in the control well (mm).

2.8 Determination of minimum inhibitory concentration (MIC)

Micro-broth dilution assay was adapted to determine the minimum inhibitory concentration (MIC) of the AuNSs against the *F. oxysporum*. MIC was defined at the lowest concentration of the AuNS to inhibit any growth completely. AuNSs treatment against *F. oxysporum* was dose-dependent (50, 60, 70, 80, 90, 100, 110, and 120 μg mL^{-1}). The lowest concentration of AuNSs against *F. oxysporum* that did not show any growth in the broth media after 48 h was referred to as the MIC. The turbidity at 595 nm of the yeast was determined by using an Agilent Cary 3500 Multicell UV-vis spectrophotometer.

2.9 SEM characterization of *F. Oxysporum*

To determine the effect of AuNSs against *Fusarium oxysporum*, the spores and hyphae cells were treated with 100 μg $μl^{-1}$ of AuNS except for the control and incubated at 28 °C for 24 h. The yeast cells treated with AuNSs were harvested for SEM analysis following a standard procedure. Briefly, the yeast cells were centrifugated at 5000 rpm for 5 min. The supernatant was discarded, the precipitates were further washed with PBS (3×), and the cells were then fixed with 2.5% glutaraldehyde for 6 h at 4 °C. The glutaraldehyde solution was discarded, and cells were isolated using a different ethanol mixture of 0, 50, 70, 90, 95, and 100%. Finally, the yeast cells were freeze-dried and mounted for the SEM visualization.[29]

2.10 Statistical analysis

All experiments were performed in triplicates and the statistical results are reported as mean ± standard deviation (SD). The results were subjected to one-way analysis of variance (ANOVA) using origin 8 with a $p < 0.05$ considered statistically significant.

3 Results and discussion

3.1 Optical characterization of anisotropic gold nanoparticles

The gold nanostars were synthesized at room temperature by reducing gold ions using QPABA without any surfactant. The one-pot technique for synthesizing AuNSs in this study possesses advantages that include eco-friendly, rapid, facile, and controlled morphology and sizes without using non-toxic

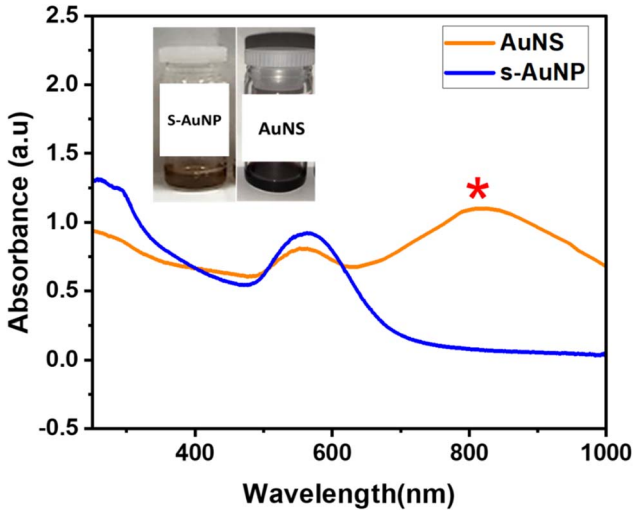

Fig. 1 UV-vis spectra of gold nanostars and spherical gold nanoparticles synthesized with QPABA and gold precursor at a molar ratio of 2 : 1 and 1 : 1, respectively.

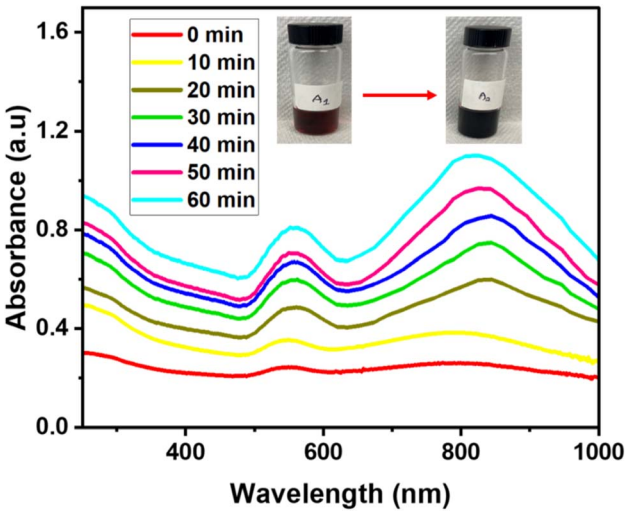

Fig. 2 UV-vis spectra showing the growth process of gold nanostars derived from QPABA and gold precursor in the molar ratio of 2 : 1. The duration of growth occurred over the range of 1 hour.

materials.[30] The effect of QPABA on the morphological characteristics of AuNSs was investigated by varying the concentration of QPABA. QPABA acts as a capping agent and reducing agent for synthesizing AuNSs. Aqueous synthesis of star-shaped and spherical gold nanoparticles using QPABA was monitored using Agilent Cary 3500 Multicell UV-vis spectrophotometer. It is worth noting that the formation of spherical gold nanoparticles and gold nanostars were achieved by maintaining a molar ratio of 1 : 1 and 2 : 1 for QPABA and the gold precursor, respectively.[19] The solution gradually changed from light brown to deep wine, indicating the formation of AuNSs as seen in Fig. 1 (inset). The color change is attributed to the excitation of the surface plasmon vibrations, indicating nano-stars formation. The reaction was completed in 1 h.

The characteristic SPR band observed at 540 nm increased with an increase in the concentration of QPABA. This effect eventually led to the formation of star-shaped gold nanoparticles with an SPR peak at 800 nm. The peaks formed by the QPABA-Au^{3+} observed in the UV-visible spectroscopic analyses confirmed the uniform size and shape of the nanoparticles. The corresponding UV-vis absorption spectrum shows two characteristic bands centered at 550 and 800 nm which corresponds to the localized surface plasmon resonances (LSPR) of the cores and the tip of the gold nanostars, respectively.[31] Notably, the size and shape of AuNPs have influences on the surface plasmon resonance (SPR) band, stability, color, and optical absorption intensity.

3.2 Kinetic growth process of anisotropic gold nanostars

To understand the growth process of gold nanostars, time-course measurements of the UV-vis spectroscopy was adapted to monitor the formation of nanoparticles and the evolution of shapes that lead to star formation. The color change from the initial reaction solution was time-dependent.[19] The color transitioned from a pale wine solution to a dark wine color. The color transitions corresponded to the formation of gold nanostars. The resultant plasmon resonance peak for the appearance of the nanostars was located at 800 nm. The experimental setup for synthesizing gold nanostar was sampled at 10 min intervals for UV-vis analysis. Given the duration of synthesis, the reaction mixture after 1 h growth duration led to a constant appearance of SPR peak at 800 nm, hence the formation of gold nanostars. The mechanism of AuNSs initially entails the formation of primary particles *via* the reduction of $HAuCl_4$ by QPABA, acting as the preferential reducing and capping agent. Then, these particles aggregate *via* surface interaction and then act as the template assisting the anisotropic growth of gold in favorable directions, with a resultant formation of AuNSs. Maintaining a 2 : 1 ratio of QPABA to the gold precursor favors the growth of gold nanostar. The initial reaction entails the rapid formation of spherical gold nanoparticles. The higher concentration of the QPABA drives the formation of the star shape. Controlling the growth mechanism of the gold nanostar was attributed to the reducing power of the QPABA. The particle growth at the (111) index plane of the nuclei further confirmed the gold nanostar. The as-prepared AuNSs anisotropic growth mechanism possessed unique surface morphology that correlates to its plasmon resonance with abundance protrusions and edges for several applications (Fig. 2).

3.3 TEM characterization of anisotropic gold nanoparticles

The morphology of the as-prepared AuNSs was analyzed by the high-resolution TEM in a normal mode. The as-prepared NPs were found to be stable for more than six months without any precipitation. The TEM images showed spherical particles and sizes dependent on the concentration of QPABA.

The average particle size of the spherical nanoparticles is 25.7 ± 2 nm, as seen in Fig. 3E and F. The spherical nanoparticles were derived from a molar ratio of 1 : 1 between QPABA and gold ions. Fig. 3A–C shows images of AuNSs of varying

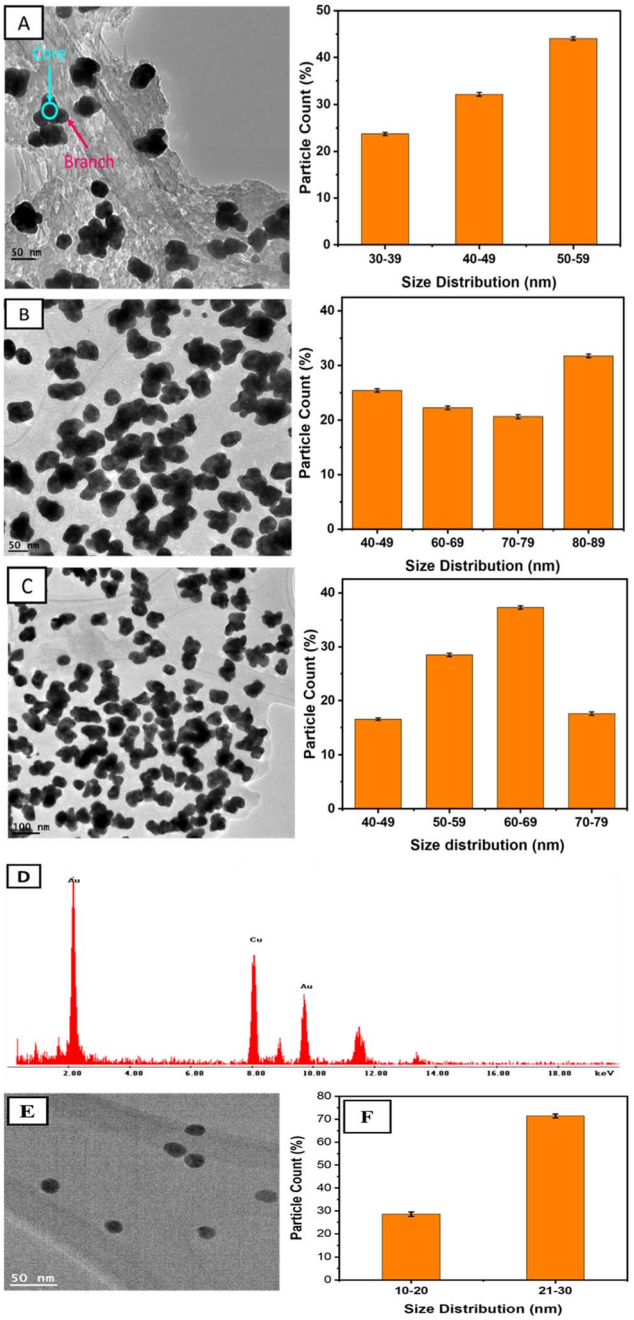

Fig. 3 (A–C) High-resolution TEM images of QPABA-derived gold nanostars and their corresponding histogram of the size distribution. (D) Energy-dispersive X-ray (EDX) elemental spectrum of gold nanostars (E) spherical gold nanoparticles obtained from a 1 : 1 ratio of QPABA and Au^{3+} ions. (F) Size distribution histogram of spherical gold nanoparticles.

diameters obtained by a 2 : 1 molar ratio of QPABA to gold precursors. As seen in the TEM micrographs, the resultant particles exhibit anisotropy and are uniform with a unique morphology of a peculiar star-like structure.[19] TEM images shown in Fig. 3C indicate that nanostars are 40 nm in dimension. Fig. 3A shows that the nanostars consist of a core and obtuse branches originating from the core. The synthesized AuNSs in Fig. 3A–C were found to have average crystallite sizes of 52 ± 3 nm, 40 ± 2 nm, and 58 ± 2 nm, respectively. The morphology of these gold nanostars provides a myriad of applications for the treatment of resistant microbial infections.[32] The EDX was used to characterize the elemental mapping of the synthesized gold nanostars.[33] The EDX profile of the as-prepared gold nanostars shows that the AuNSs are composed of Au, C, O, and Cu. In Fig. 3D, the EDX confirmed that the gold element was the predominant component of the gold nanostar. The Cu peak signal originated from copper–carbon grid. The source of oxygen and carbon originates from the QPABA ligand. The XRD patterns identified the crystal structure of the as-synthesized gold nanostars as face-centered-cubic.[33]

As seen in Fig. 4A, four distinct peaks observed at 38.2°, 44.4°, 64.6°, and 78° in the 2θ range of 20–85 °C were ascribed to (1 1 1), (2 0 0), (2 2 0), (3 1 1) indexes, respectively. Notably, the ratio intensity between the (111) and the (200) diffraction is given as 0.32. Since (111) is the highest peak, we can conclude that the preferential growth of gold nanoparticles occurs along the (111) direction.[13] The face-centered cubic (fcc) structure of the gold nanostars matches the Joint Committee on Powder Diffraction Standard (JCPDS) card number 00-004-084.[13] The Selected Area Electron Diffraction (SAED) pattern of a single gold nanostar in Fig. 4B shows the ring patterns which indicate the crystallinity of the as-prepared AuNSs. The rings of the SAED confirm the crystal structure of the gold nanostars, as confirmed by the XRD.

3.4 Mechanism of gold nanostars formation using QPABA

Synthetic methods to control the formation of Au nanostars are limited. Nanostars are characterized by an uncertain number of protrusions from their core. In this study, the even formation of monodispersed gold nanostars is achieved by varying concentrations of QPABA. The QPABA plays a shape-determining role in particle morphology owing to its strong reducing and stabilizing capability. The mechanistic growth and formation of gold nanostars are shown in Scheme 3. QPABA reacts with $HAuCl_4$ in a 1 : 1 ratio and forms the Au seeds instantaneously. The reducing capacity of QPABA is slower at low concentrations and the gold seeds are more prominent. The nucleation rate of the Au (0) is rapid when the concentration of QPABA is high; as a result, Au seeds of smaller sizes are synthesized. The TEM results suggest that during the first stage of the reaction, the nuclei growth of gold ions occurs in the presence of the weak binding of low-concentrated QPABA. The 1 : 1 ratio of QPABA and $HAuCl_4$ yields a spherical gold SPR band at 540 nm. Furthermore, the 2 : 1 ratio of QPABA and $HAuCl_4$ leads to an LSPR at 800 nm. The increased amount of QPABA leads to strong interaction and reduction of the gold ions.[31] The excess QPABA facilitates the growth of gold seeds from the nucleation phase into star-shaped nanoparticles. Notably, as the protrusions from the core of the nanostar increase in length, the degree of hybridization between the core and branch plasmons increases. A redshift confirms this strong interaction and hybridization at 800 nm. The even formation of the nanostars

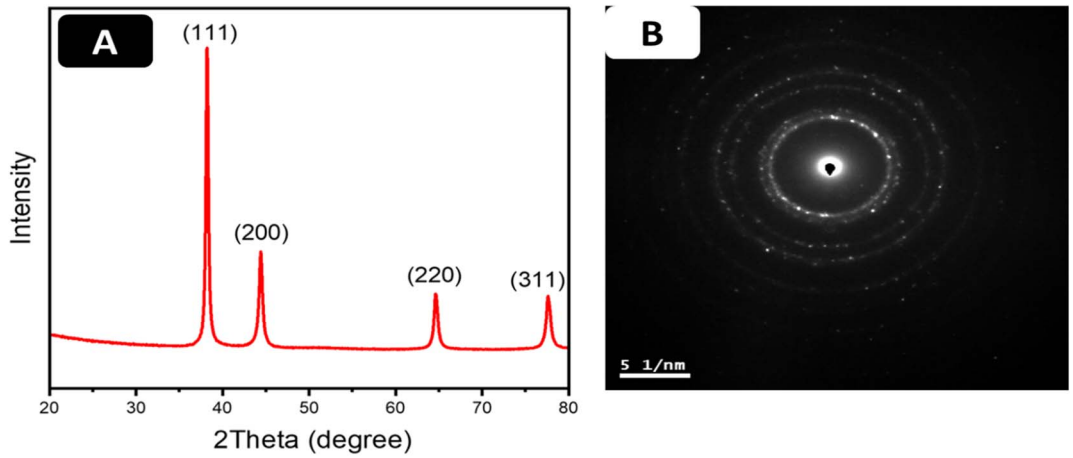

Fig. 4 (A) XRD pattern of AuNS controlled synthesized with 5 mM QPABA. (B) Selected area electron diffraction (SAED) pattern of gold nanostars.

shows the stabilizing capacity and control of QPABA, orchestrating the formation of the resultant star-shaped particle with myriad applications.

3.5 Comparative analysis of QPABA to different reducing agents

Shape-directing agents for the formation of anisotropic gold nanoparticles and their corresponding applications have been identified in Table 2. Some of these shape-directing agents act as either reducing or capping agents. It has been reported that several factors, such as synthetic method, choice of solvent, and reducing and capping agents play a role in the fabrication of anisotropic nanomaterial.[34,35] We highlight some of the reducing agents and the synthetic approach for formulating gold nanostars. Cetyltrimethylammonium bromide (CTAB) is not eco-friendly, and its application in synthesizing anisotropic nanomaterials may render them toxic.[36] We seek to promote the greener synthesis of gold nanostars by using plant-based phytochemicals as reducing agents at room temperature.

QPABA is a quercetin derivative and was synthesized to improve its polar solubility. It was produced *via* facile two-step reductive amination. Applying QPABA in the anisotropic synthesis of gold nanostars exhibits a greener approach for utilizing safe reducing agents. QPABA is compared to other reducing agents to determine its reducing and stabilizing

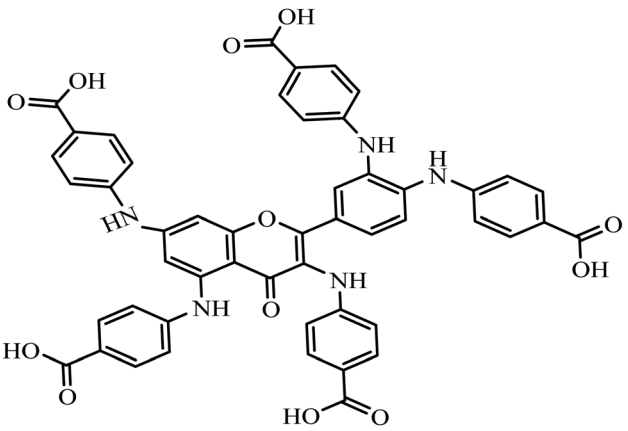

Scheme 1 Structure of quercetin-*para*-aminobenzoic acid (QPABA).

Table 2 Comparative analysis of shape-directing reducing agent/capping agent for the synthesis of gold nanostars and their applications

Shape-directing reducing agent	Synthetic method	Sizes (diameter)	Application	References
Gelatin	Au-salt (3 mM) reacts with (0.5%) of gelatin at acidic pH (3–6)	~60 nm	Human lung cancer cells (A549)	Das *et al.*[37]
Hydroxylamine	A solution of $HAuCl_4$ solution was added to hydroxylamine was a solution at pH 12	42 nm	Sensing and biomedical application	Minati *et al.*[38]
Cetyltrimethylammonium bromide (CTAB)	Gold seeds stabilized using CTAB solution	6 nm	Inhibition of melanoma B16–F10 cells	Navarro *et al.*[39]
2-[4-(2-Hydroxyethyl)-1-piperazinyl] propane sulfonic acid (EPPS)	$AuCl_4$ reacts with EPPS buffer	6–8 nm	Detection of uranyl	Harder *et al.*[40]
QPABA	5 mM QPABA reacts with 0.1 mM $HAuCl_4$	44 nm	Inhibition of *Fusarium oxysporum*	This study

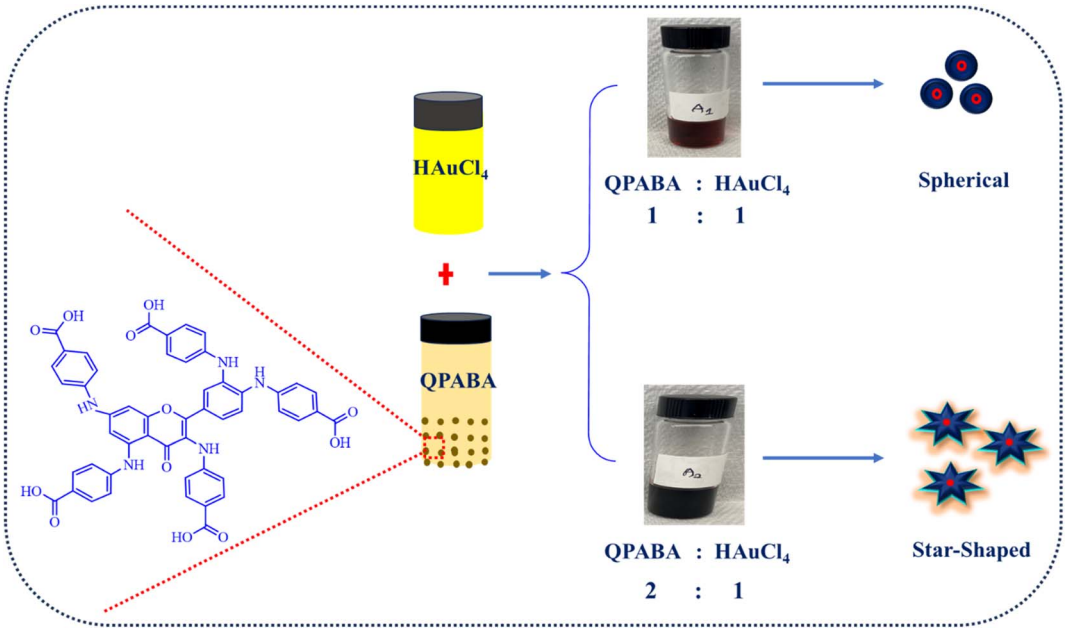

Scheme 2 Synthesis of anisotropic gold nanoparticles using QPABA.

capacity as natural derivatized quercetin. QPABA has several binding sites for interacting with gold ions. The strength of the interaction determines the ability to both reduce and stabilize the growth of the star-shaped nanoparticles. As shown in Scheme 1, there are several potential sites of binding: carboxyl groups in proximity to the gold ions in solution, there are amide groups in Ring B, that are easily oxidized. The functional groups in Ring A could be farther and unavailable for binding. The orientation and steric hindrance of the functional groups in QPABA could impact their binding to gold ions. Depending on the molecular geometry, the carboxyl groups in proximity may interact directly with the gold atoms leading to low-energy stabilized structures. Such possibilities are needed to explain the unusual stability observed in the resulting AuNSs. Hence computational studies were employed to give a better insight into the interactions.

3.6 Computational analysis of QPABA-derived AuNS

In this study, optimized structures of QPABA ligand and QPABA – Au^{3+} structures (MS1-5) and corresponding energies were determined. The different conformational optimized structures are shown in Fig. 5. To understand the effects of the energy in

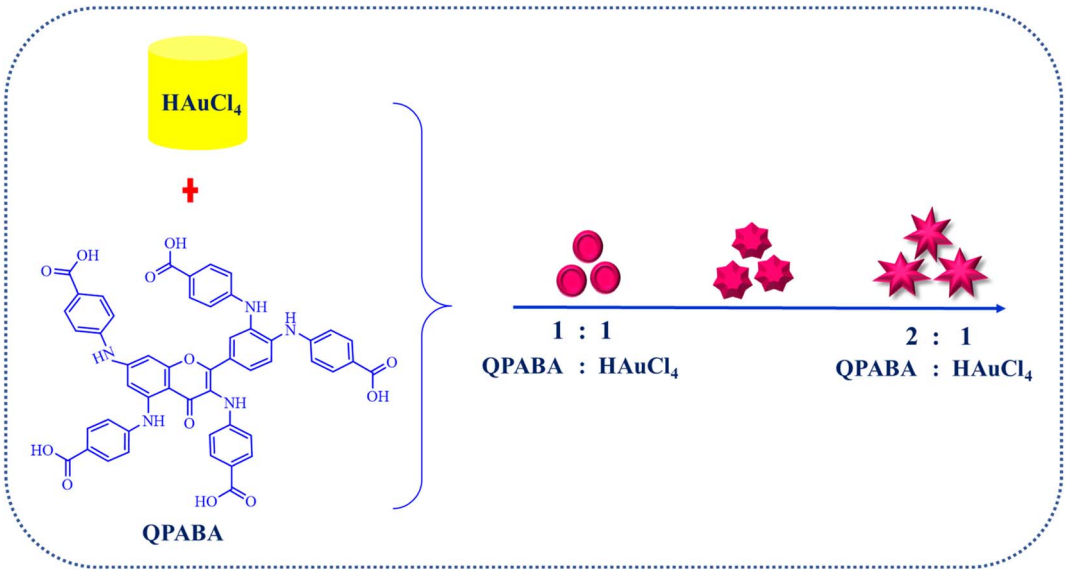

Scheme 3 Mechanistic formation of gold nanostars in increasing QPABA.

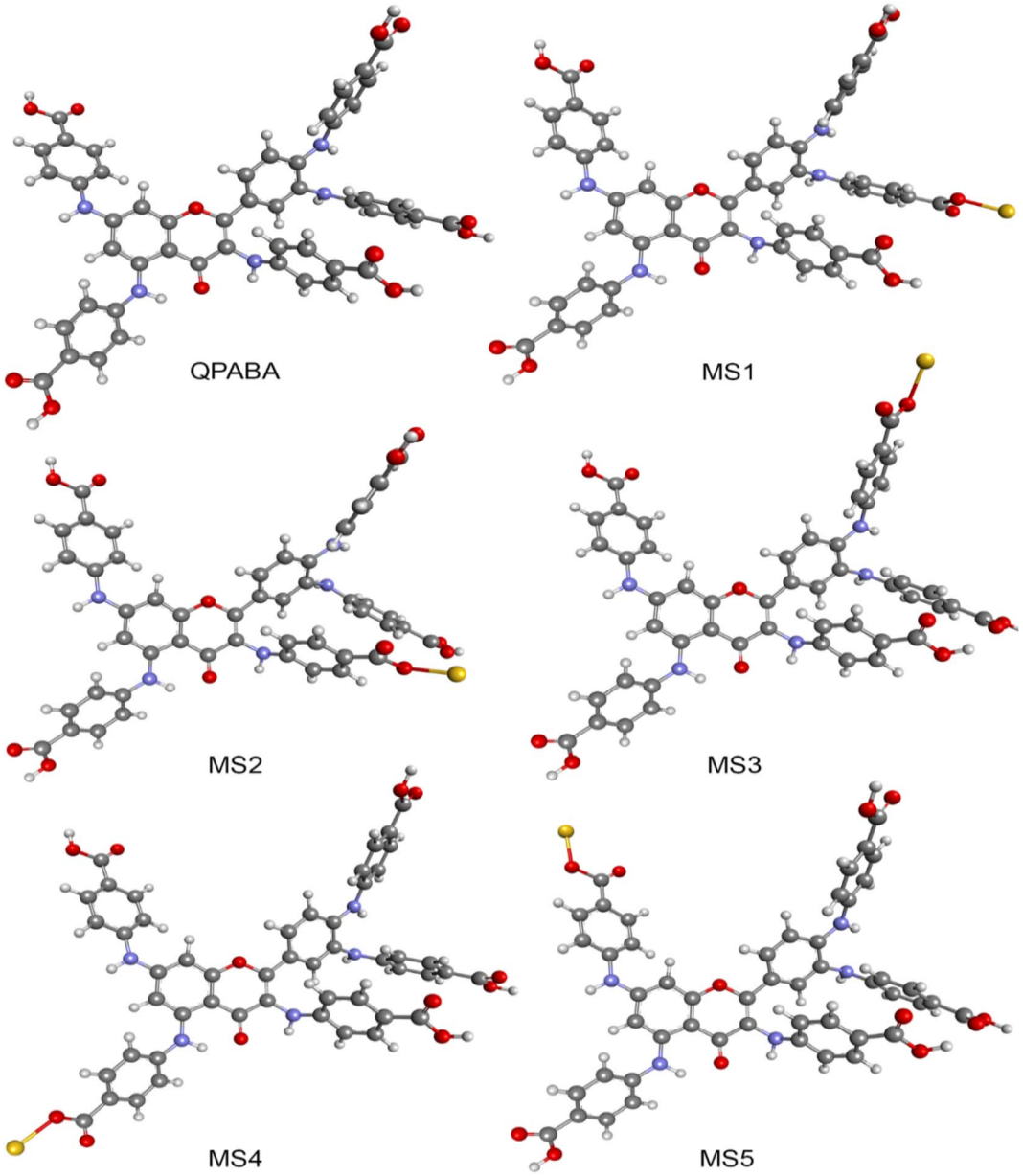

Fig. 5 Optimized structures of QPABA and QPABA–Au nanocomposite model structures (MS1-5).

the formation of a specific configuration, we performed a geometrical optimization of the QPABA and gold complex to determine their stability. Fig. 6 shows the binding energies for the different calculated models. It is worth stating that the morphology of AuNSs depends on the concentration of the reducing agent used in the reduction process. The stability of the nanoparticles is evaluated using density functional theory based on quantum mechanical calculations.[20,41] The minimum energy for each of the structures was obtained utilizing a geometry optimization task based on the DFT method. The geometry optimization was followed by a single-point energy calculation to obtain the energies of the various QPABA-gold conformations. The energies corresponding to possible QPABA–Au nanocomposite structures (MS1-5) were calculated to obtain the most stable structure among all possible structures. The results showed that the energy corresponding to the most stable nanocomposite model structure (MS2) was found to be -1.29222×10^7 kJ mol^{-1} among all possible structures. To understand the stabilizing role of QPABA in the synthesis of gold nanostars, the three-dimensional structure and binding mode of carboxylate-containing ligand (QPABA) to gold ions have been determined using computational modeling.[42]

The binding effect between the QPABA and the gold ions occurs at positions 3 and 4 OH-rich regions of QPABA. The OH site for gold reduction is favored at high QPABA to gold ratios. The interactions between gold and QPABA occur through coordination bonds. Since QPABA has different OH sites for reducing the gold ions, the DFT calculation showed that the

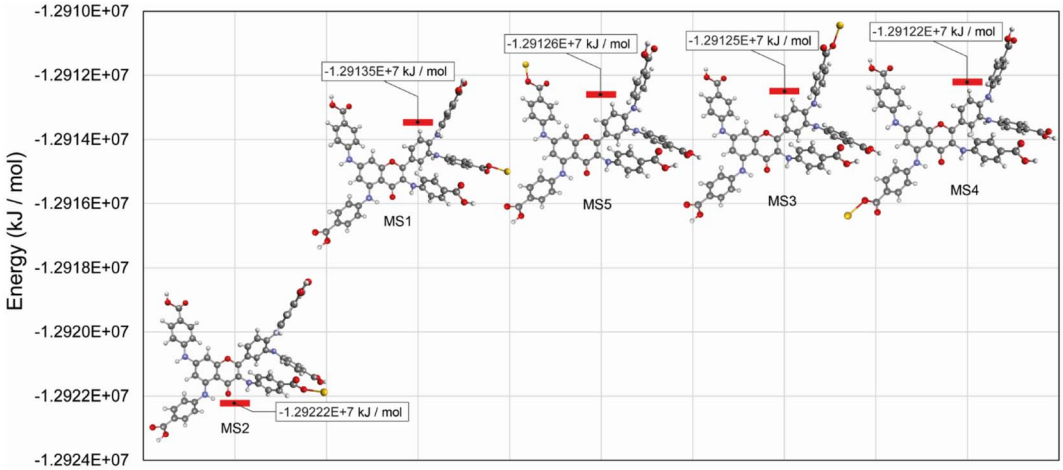

Fig. 6 Possible QPABA–Au^{3+} nanocomposite model structures and corresponding energies.

stable conformer (MS2) is the favorable configuration of QPABA for reducing gold ions.

The different interaction energy (E_{int}) between gold ions and the different OH sites on the QPABA is displayed in Fig. 6. In the present work, E_{int} for the QPABA–gold complex was modeled after a mono-substitution of the hydrogen atoms of each hydroxyl group before interaction with gold ions.[20] A comparison of E_{int} values shows that the interaction energies of the most favorable QPABA–Au complex bonds are -1.29222×10^7 kJ mol^{-1}. The highest stability of the resultant QPABA-Au^{3+} complex was attributed to the intramolecular bonding between the OH groups and the gold ions. Several reports have identified the poor stability of different metallic nanostars.[43,44] Wu *et al.* reported that the fabrication of anisotropic gold nanoflowers transformed into isotropic spherical gold nanoparticles within 1 h owing to the thermodynamically unstable character of nanoflowers.[45] The formation and stability of the nanostars are determined by the reducing and capping agent and the reaction conditions. The QPABA acting as both reducing and capping agents shows a high stability for the fabrication of gold nanostars due to intra-H bonding and using water as a solvent at room temperature.

3.7 Antifungal activity of AuNSs against *F. oxysporum*

Fusarium wilt caused by *F. oxysporum* deteriorates the quality of plants. The pathogen can survive for a long time and inflict a significant loss of agricultural produce.[46] There is a need for inexpensive management of fusarium wilts outbreaks. The agar well diffusion assay was performed to determine the mycelial growth inhibition activity of the star-shaped gold nanoparticles against *F. oxysporum*. The effect of AuNS treatment on the mycelial growth of *F. oxysporum* strains were tested for 7 days of incubation. The growth of *F. oxysporum* with and without exposure to AuNSs are shown in Fig. 7.

Table 3 Zone of inhibition (mm) after AuNS treatment against *F. oxysporum* in a dose-dependent manner

		Zone of inhibition (mm)	
Fungus	AuNS treatment (μg mL^{-1})	Day 2	Day 5
F. oxysporum	Control	0.00 ± 0.00	0.00 ± 0.00
	75	7.20 ± 0.70	8.20 ± 0.56
	100	11.00 ± 1.20	12.20 ± 0.45
	125	14.90 ± 0.90	15.2 ± 0.63

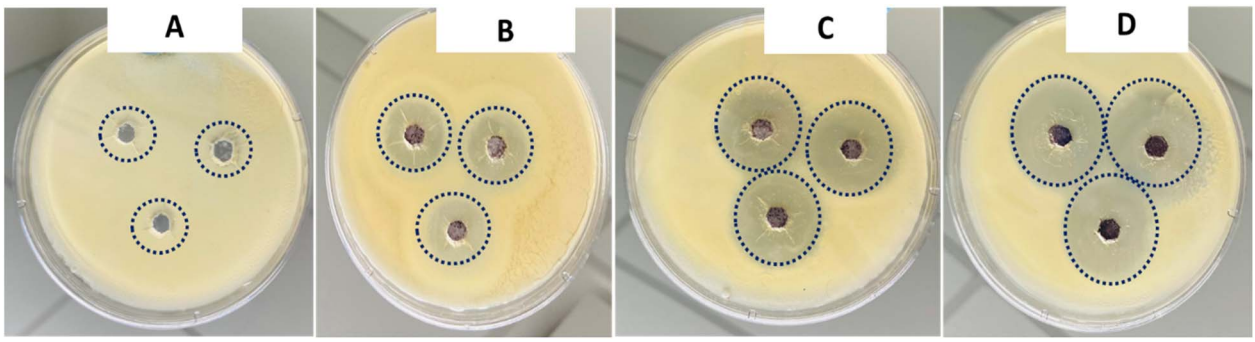

Fig. 7 Antifungal dose-dependent treatment of QPABA-derived *F. oxysporum*. Control did not receive the treatment of AuNS, but just the reducing/capping agent, QPABA. (A) Control (B) 75 μg mL^{-1}, (C) 100 μg mL^{-1}, and (D) 125 μg mL^{-1}.

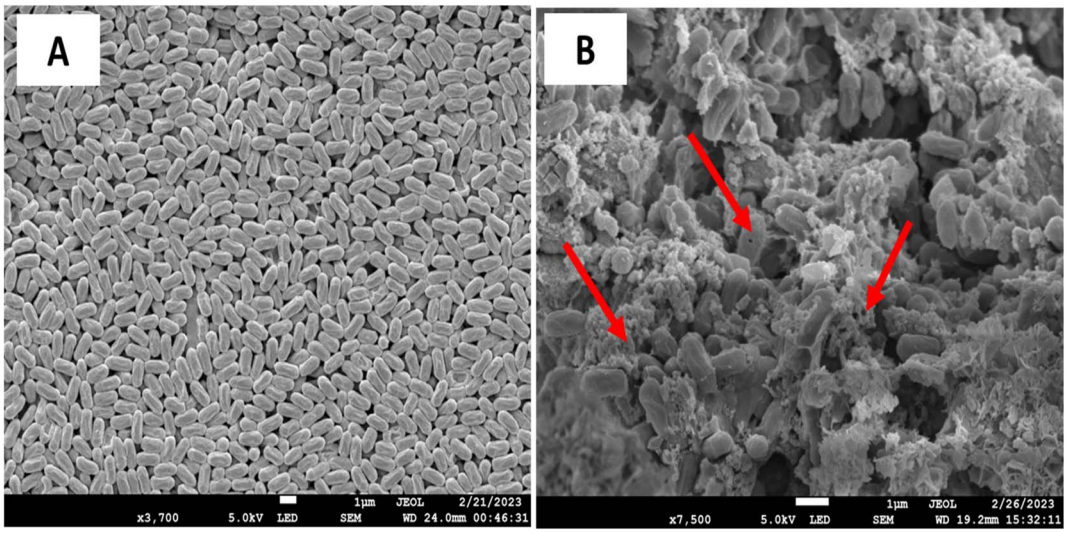

Fig. 8 SEM analysis of before (A) and after treatment of 75 μg mL^{-1} of AuNS. Arrows show the disintegrated membrane of the *F. oxysporum*.

The cells (10^6 cells per CFU) were treated with AuNSs in a dose-dependent manner (75 μg mL^{-1}, 100 μg mL^{-1}, and 125 μg mL^{-1}). From our results, it was obvious that AuNSs significantly reduced the mycelial growth after 7 days as compared with the untreated controls. Fig. 7 shows that increasing the concentration treatments of AuNS corresponded to an increase in the zone of inhibition. The zone of inhibition represents the efficacy of the AuNSs. The zones of inhibition were used to estimate the susceptibility of AuNSs to *F. oxysporum*.[28] From the results, treatment of AuNS at 125, 100, and 75 μg mL^{-1} yielded a reduction in mycelial growth that corresponded to the zone of inhibitions of 15.2 ± 0.63 mm, 12.20 ± 0.45 mm, and 8.20 ± 0.56 mm respectively. It was obvious that higher dose treatment yielded higher zones of inhibition. The zones where *F. oxysporum* did not grow correlated to the MIC after the minimum treatment of the AuNS. This approach aided the selection of the appropriate concentration of the AuNS treatment for *F. oxysporum*. The MIC of AuNS against *F. oxysporum* was 100 μg mL^{-1}, and this represents the lowest concentration for treatment. Nevertheless, treatment using spherical gold nanoparticles following the treatment procedure illustrated above did not show inhibition of the mycelia growth. In this sense, we can conclude that the nanostar shape influences the antifungal activity against *F. oxysporum*.

The measured diameter of inhibition zones around each diffusion well after treatment of the AuNSs is shown in Table 3. Some factors that contributed to the antifungal activity included concentration, small particle size, and morphology of the nanoparticles. It is worth noting that, at constant dosage treatment and sizes for both spherical and star-shaped gold nanoparticles, the effectiveness of the nanostars was more pronounced compared to the spherical gold nanoparticles.[30] In this view, it was concluded that the shape of the resultant particles played a role in the mycelia reduction of *F. oxysporum* (Table 2).

3.8 SEM analysis of *F. oxysporum* after AuNSs treatment

SEM microscopy was used to assess whether the AuNSs impacted the growth and morphological transformation of the *F. oxysporum*. From Fig. 8A, the control without treatment showed rapid mycelial growth of *F oxysporum* after 48 h of incubation at 28 °C. In contrast, the treatment of AuNS (100 μg mL^{-1}) showed morphological changes, as seen in Fig. 8B. Thus, the results strongly suggest that AuNSs can effectively inhibit the growth of *F. oxysporum*.

The mechanism of antifungal activity can be attributed to the morphology and high surface-to-volume ratio of AuNSs with an increased affinity to interact with the fungi, hence the antifungal activity of AuNSs against *F. oxysporum* is effective. Furthermore, the antifungal mechanism of NPs is ascribed to other factors, such as the absorption and accumulation of ions in the fungal cell, which damages the cell membrane enzymes.[47] SEM showed significant morphological alterations in *F. oxysporum* upon exposure to AuNPs. The morphological change in structure leads to fungal cell death. These data are consistent with reported data that shows that the effects of AuNPs on *F. oxysporum* disrupt the cell membrane and organelles. Furthermore, another possible mechanism of action for AuNS demonstrated against fusarium has been reported by Xie *et al.*[48,49] The AuNS treatment disintegrated the cells with their sharp edges that eventually killed the fungi. Together, these results suggest that the antifungal mechanism of gold nanostars is influenced by the concentration of gold ions and the size and morphology of particles. Our results are consistent with data reported elsewhere.[50,51]

4 Conclusion

The shape-controlling capacity of the quercetin derivative QPABA has been demonstrated as a greener and low-cost reducing and capping agent for synthesizing gold nanostars

with high yield. The resultant AuNSs were characterized by TEM, UV-vis, XRD, and EDX to confirm the morphology, size, and crystallinity of the particles and shape evolution of gold nanostars. The computational analysis confirmed the structural conformation and stability of the QPABA and gold ions to form gold nanostars. The theoretical analysis proved that the formation of the AuNSs was ascribed to the conformational interaction between gold ions and QPABA at positions 3 and 4 in addition to factors such as the concentration of the ligand and choice of solvent. The antifungal activity of the AuNSs was effective against *F. oxysporum* at a MIC of 100 μg mL^{-1}. Our study shows the site-specific interaction between gold ions and QPABA for the synthesis of anisotropic gold nanoparticles to treat agricultural-based fungal infections. The future work will focus on the influence of shape on the cytotoxicity of gold nanostars against MCF-7 human breast cancer cell lines. Since cytotoxicity is a measure of biocompatibility,[52] it is expected that the morphological properties of the gold nanostars will play a role in determining the cytotoxicity effects against breast cancer cell lines. This will enlighten and contribute to the established biocompatibility of star-shaped gold nanoparticles.

Conflicts of interest

There are no conflicts of interest to declare.

Acknowledgements

The authors acknowledge the US National Science Foundation Grant #IOS-1543944, NJIT Start-ups (172803), and the Bill & Melinda Gates Foundation for funding. The computational studies reported in this paper were partially performed at TUBITAK ULAKBIM, High Performance and Grid Computing Center (TRUBA resources), and Kocaeli University.

References

1 H. M. Ji, H. Y. Mao, S. J. Li, T. Feng, Z. Y. Zhang, L. Cheng, S. J. Luo, K. A. Borkovich and S. Q. Ouyang, *New Phytol.*, 2021, **232**, 705–718.
2 H. Ashraf, T. Anjum, S. Riaz, I. S. Ahmad, J. Irudayaraj, S. Javed, U. Qaiser and S. Naseem, *Environ. Sci.: Nano*, 2021, **8**, 1729–1748.
3 O. Degani and B. Kalman, *J. Fungi*, 2021, **7**, 235.
4 X. Huang, J. Zhao, X. Zhou, Y. Han, J. Zhang and Z. Cai, *Eur. J. Soil Sci.*, 2019, **70**, 518–529.
5 M. A. Khan, S. A. Khan, U. Waheed, M. Raheel, Z. Khan, A. F. Alrefaei and H. H. Alkhamis, *J. King Saud Univ., Sci.*, 2021, **33**, 101299.
6 H. Shang, C. Ma, C. Li, J. Zhao, W. Elmer, J. C. White and B. Xing, *Environ. Sci. Technol.*, 2021, **55**, 13432–13442.
7 K. Giannousi, A. Pantazaki and C. Dendrinou-Samara, in *Nanostructures for Antimicrobial Therapy*, Elsevier, 2017, pp. 515–529.
8 R. Yazdian-Robati, N. Hedayati, S. Dehghani, M. Ramezani, M. Alibolandi, M. Saeedi, K. Abnous and S. M. Taghdisi, *Anal. Biochem.*, 2021, **629**, 114307.
9 C. T. Campbell, J. C. Sharp, Y. Yao, E. M. Karp and T. L. Silbaugh, *Faraday Discuss.*, 2011, **152**, 227–239.
10 F. J. Osonga, G. Eshun, S. Kalra, I. Yazgan, L. Sakhaee, R. Ontman, S. Jiang and O. A. Sadik, *ACS Agric. Sci. Technol.*, 2022, **2**, 42–56.
11 J. C. L. Chow, in *Handbook of Functionalized Nanomaterials*, Elsevier, 2021, pp. 281–308.
12 J. A. Moore and J. C. Chow, *Nano Express*, 2021, **2**, 022001.
13 F. J. Osonga, V. M. Kariuki, V. M. Wambua, S. Kalra, B. Nweke, R. M. Miller, M. Cesme and O. A. Sadik, *Acs Omega*, 2019, **4**, 6511–6520.
14 S. Siddique and J. C. Chow, *Nanomaterials*, 2020, **10**, 1700.
15 N.-f. Sun, Z.-a. Liu, W.-b. Huang, A.-l. Tian and S.-y. Hu, *Crit. Rev. Oncol./Hematol.*, 2014, **89**, 352–357.
16 Y. Xiao, Y. Li, Y. Shi, Z. Li, X. Zhang, T. Liu, T. H. Farooq, Y. Pan, X. Chen and W. Yan, *Sci. Total Environ.*, 2022, **806**, 151211.
17 A. Candreva, F. Parisi, R. Bartucci, R. Guzzi, G. Di Maio, F. Scarpelli, I. Aiello, N. Godbert and M. La Deda, *Chemistryselect*, 2022, **7**, e202201375.
18 L. Wei, T. Sheng, J.-Y. Ye, B.-A. Lu, N. Tian, Z.-Y. Zhou, X.-S. Zhao and S.-G. Sun, *Langmuir*, 2017, **33**, 6991–6998.
19 F. J. Osonga, G. B. Eshun and O. A. Sadik, *RSC Adv.*, 2022, **12**, 31855–31868.
20 A. Jakhmola, R. Vecchione, F. Gentile, M. Profeta, A. Manikas, E. Battista, M. Celentano, V. Onesto and P. Netti, *Mater. Today Chem.*, 2019, **14**, 100203.
21 F. J. Osonga, A. Akgul, R. M. Miller, G. B. Eshun, I. Yazgan, A. Akgul and O. A. Sadik, *ACS Omega*, 2019, **4**, 12865–12871.
22 F. J. Osonga, J. O. Onyango, S. K. Mwilu, N. M. Noah, J. Schulte, M. An and O. A. Sadik, *Tetrahedron Lett.*, 2017, **58**, 1474–1479.
23 C. E. Chang and M. K. Gilson, *J. Comput. Chem.*, 2003, **24**, 1987–1998.
24 M. J. Frisch, G. W. Trucks, H. B. Schlegel, G. E. Scuseria, M. A. Robb, J. R. Cheeseman, G. Scalmani, V. Barone, G. A. Petersson, H. Nakatsuji, X. Li, M. Caricato, A. V. Marenich, J. Bloino, B. G. Janesko, R. Gomperts, B. Mennucci, H. P. Hratchian, J. V. Ortiz, A. F. Izmaylov, J. L. Sonnenberg, D. Williams-Young, F. Ding, F. Lipparini, F. Egidi, J. Goings, B. Peng, A. Petrone, T. Henderson, D. Ranasinghe, V. G. Zakrzewski, J. Gao, N. Rega, G. Zheng, W. Liang, M. Hada, M. Ehara, K. Toyota, R. Fukuda, J. Hasegawa, M. Ishida, T. Nakajima, Y. Honda, O. Kitao, H. Nakai, T. Vreven, K. Throssell, J. A. Montgomery Jr, J. E. Peralta, F. Ogliaro, M. J. Bearpark, J. J. Heyd, E. N. Brothers, K. N. Kudin, V. N. Staroverov, T. A. Keith, R. Kobayashi, J. Normand, K. Raghavachari, A. P. Rendell, J. C. Burant, S. S. Iyengar, J. Tomasi, M. Cossi, J. M. Millam, M. Klene, C. Adamo, R. Cammi, J. W. Ochterski, R. L. Martin, K. Morokuma, O. Farkas, J. B. Foresman and D. J. Fox, *Gaussian 16, Revision C.01*, Gaussian, Inc., Wallingford, CT, 2016.
25 G. M. Barca, C. Bertoni, L. Carrington, D. Datta, N. De Silva, J. E. Deustua, D. G. Fedorov, J. R. Gour, A. O. Gunina and E. Guidez, *J. Chem. Phys.*, 2020, **152**, 154102.

26 P. Nidhi, R. Rolta, V. Kumar, K. Dev and A. Sourirajan, *J. Ethnopharmacol.*, 2020, **262**, 113135.
27 S. Magaldi, S. Mata-Essayag, C. H. De Capriles, C. Pérez, M. Colella, C. Olaizola and Y. Ontiveros, *Int. J. Infect. Dis.*, 2004, **8**, 39–45.
28 S. Raj, V. Vinod, J. Jayakumar, P. Suresh, A. Kumar and R. Biswas, *Lett. Appl. Microbiol.*, 2021, **73**, 31–38.
29 C. Zhao, X. Lv, J. Fu, C. He, H. Hua and Z. Yan, *J. Appl. Microbiol.*, 2016, **121**, 254–262.
30 F. J. Osonga, I. Yazgan, V. Kariuki, D. Luther, A. Jimenez, P. Le and O. A. Sadik, *RSC Adv.*, 2016, **6**, 2302–2313.
31 A. Kedia and P. S. Kumar, *J. Mater. Chem. C*, 2013, **1**, 4540–4549.
32 M. Borzenkov, G. Chirico, L. d'Alfonso, L. Sironi, M. Collini, E. Cabrini, G. Dacarro, C. Milanese, P. Pallavicini and A. Taglietti, *Langmuir*, 2015, **31**, 8081–8091.
33 R. P. Talemi, S. M. Mousavi and H. Afruzi, *Mater. Sci. Eng., C*, 2017, **73**, 700–708.
34 K. Vijayaraghavan and T. Ashokkumar, *J. Environ. Chem. Eng.*, 2017, **5**, 4866–4883.
35 M. L. Personick and C. A. Mirkin, *J. Am. Chem. Soc.*, 2013, **135**, 18238–18247.
36 J. S. Bozich, S. E. Lohse, M. D. Torelli, C. J. Murphy, R. J. Hamers and R. D. Klaper, *Environ. Sci.: Nano*, 2014, **1**, 260–270.
37 R. P. Das, V. V. Gandhi, B. G. Singh and A. Kunwar, *New J. Chem.*, 2021, **45**, 13271–13279.
38 L. Minati, F. Benetti, A. Chiappini and G. Speranza, *Colloids Surf., A*, 2014, **441**, 623–628.
39 J. R. Navarro, D. Manchon, F. Lerouge, N. P. Blanchard, S. Marotte, Y. Leverrier, J. Marvel, F. Chaput, G. Micouin and A.-M. Gabudean, *Nanotechnology*, 2012, **23**, 465602.
40 R. A. Harder, L. A. Wijenayaka, H. T. Phan and A. J. Haes, *J. Raman Spectrosc.*, 2021, **52**, 497–505.
41 H. Al-Johani, E. Abou-Hamad, A. Jedidi, C. M. Widdifield, J. Viger-Gravel, S. S. Sangaru, D. Gajan, D. H. Anjum, S. Ould-Chikh and M. N. Hedhili, *Nat. Chem.*, 2017, **9**, 890–895.
42 G. Zazeri, A. P. R. Povinelli, N. M. Pavan, D. R. de Carvalho, C. L. Cardoso and V. F. Ximenes, *J. Mol. Struct.*, 2021, **1244**, 130995.
43 W. Xi and A. J. Haes, *J. Am. Chem. Soc.*, 2019, **141**, 4034–4042.
44 S. Sasidharan, D. Bahadur and R. Srivastava, *ACS Sustainable Chem. Eng.*, 2017, **5**, 10163–10175.
45 F. Wu, Y. Liu, Y. Wu, D. Song, J. Qian and B. Zhu, *J. Mater. Chem. B*, 2020, **8**, 2128–2138.
46 W. V. Mbasa, W. A. Nene, F. A. Kapinga, S. A. Lilai and D. D. Tibuhwa, *Crop Prot.*, 2021, **139**, 105379.
47 L. Hermida-Montero, N. Pariona, A. I. Mtz-Enriquez, G. Carrión, F. Paraguay-Delgado and G. Rosas-Saito, *J. Hazard. Mater.*, 2019, **380**, 120850.
48 X. Wang, X. Liu, J. Chen, H. Han and Z. Yuan, *Carbon*, 2014, **68**, 798–806.
49 J. Xie, Z. Ming, H. Li, H. Yang, B. Yu, R. Wu, X. Liu, Y. Bai and S.-T. Yang, *Chemosphere*, 2016, **151**, 324–331.
50 M. Noman, T. Ahmed, U. Ijaz, M. Shahid, M. M. Nazir, J. C. White, D. Li and F. Song, *Small*, 2023, **19**, 2205687.
51 F. J. Osonga, A. Akgul, I. Yazgan, A. Akgul, G. B. Eshun, L. Sakhaee and O. A. Sadik, *Molecules*, 2020, **25**, 2682.
52 P. M. Favi, M. Gao, L. Johana Sepúlveda Arango, S. P. Ospina, M. Morales, J. J. Pavon and T. J. Webster, *J. Biomed. Mater. Res., Part A*, 2015, **103**, 3449–3462.